

First Results from Pan-STARRS1: Faint, High Proper Motion White Dwarfs in the Medium-Deep Fields

J. L. Tonry,¹ C. W. Stubbs,^{2,3} M. Kilic,^{2,4} H. A. Flewelling,¹ N. R. Deacon,¹ R. Chornock,²
 E. Berger,² W. S. Burgett,¹ K. C. Chambers,¹ N. Kaiser,¹ R-P. Kudritzki,¹
 K. W. Hodapp,¹ E. A. Magnier,¹ J. S. Morgan,¹ P. A. Price,⁵ R. J. Wainscoat,¹

ABSTRACT

The Pan-STARRS1 survey has obtained multi-epoch imaging in five bands (Pan-STARRS1 g_{P1} , r_{P1} , i_{P1} , z_{P1} , and y_{P1}) on twelve “Medium Deep Fields”, each of which spans a 3.3 degree circle. For the period between Apr 2009 and Apr 2011 these fields were observed 50–200 times. Using a reduced proper motion diagram, we have extracted a list of 47 white dwarf (WD) candidates whose Pan-STARRS1 astrometry indicates a non-zero proper motion at the 6σ level, with a typical 1σ proper motion uncertainty of 10 mas/yr. We also used astrometry from SDSS (when available) and USNO-B to assess our proper motion fits. None of the WD candidates exhibits evidence of statistically significant parallaxes, with a typical 1σ uncertainty of 8 mas. Twelve of these candidates are known WDs, including the high proper motion ($1.7'' \text{ yr}^{-1}$) WD LHS 291. We confirm three more objects as WDs through optical spectroscopy. Based on the Pan-STARRS1 colors, ten of the stars are likely to be cool WDs with $4170 \text{ K} < T_{\text{eff}} < 5000 \text{ K}$ and cooling ages $< 9 \text{ Gyr}$. We classify these objects as likely thick disk WDs based on their kinematics. Our current sample represents only a small fraction of the Pan-STARRS1 data. With continued coverage from the Medium Deep Field Survey and the 3π survey, Pan-STARRS1 should find many more high proper motion WDs that are part of the old thick disk and halo.

Subject headings: Galaxy: evolution – Proper Motions – White Dwarfs – Surveys: Pan-STARRS1

¹Institute for Astronomy, University of Hawaii, 2680 Woodlawn Drive, Honolulu HI 96822

²Harvard-Smithsonian Center for Astrophysics, 60 Garden Street, Cambridge, MA 02138

³Department of Physics, Harvard University, 17 Oxford Street, Cambridge MA 02138

⁴Homer L. Dodge Department of Physics and Astronomy, University of Oklahoma, 440 W. Brooks St., Norman, OK, 73019

⁵Department of Astrophysical Sciences, Princeton University, Princeton, NJ 08544, USA

1. INTRODUCTION

The oldest WDs in the Galactic disk and halo provide independent age measurements for their parent populations (Winget et al. 1987; Liebert, Dahn & Monet 1988). The major observational requirement for accurate age measurements is to have a large sample of cool, old WDs. However, the intrinsic faintness of the coolest WDs make them difficult to observe, and the previous studies of the Galactic disk and halo suffer from small samples of cool WDs.

The most commonly used sample of cool WDs in the Galactic disk includes 43 stars and gives an age of 8 ± 1.5 Gyr (Leggett et al. 1998). Kilic et al. (2006, 2010), Harris et al. (2006), and Rowell & Hambly (2011) significantly improved the disk WD sample based on the SDSS + USNO-B (Munn et al. 2004) or SuperCOSMOS proper motions. However, the ≈ 19.7 mag limit of the Palomar Observatory Sky Survey and the Schmidt plates do not allow the identification of many faint thick disk and halo WDs. In order to overcome the magnitude limit imposed by the plate astrometry, Liebert et al. (2007) initiated a large proper motion survey down to $r = 21$ mag. Kilic et al. (2010) identify several halo WD candidates in that survey and demonstrate that deep, wide-field proper motion surveys ought to find many halo WDs.

Classification of a WD as a halo object solely based on large proper motions can be misleading. Oppenheimer et al. (2001) identified 38 WDs as halo objects based on SuperCOSMOS proper motions and colors. However, these claims were later rejected by kinematic and detailed model atmosphere analysis. Reid et al. (2001) demonstrated that the Oppenheimer et al. (2001) sample is more consistent with the high-velocity tail of the thick disk component. In addition, Bergeron (2003) finds that these WDs are too warm and too young to be members of the Galactic halo. Bergeron et al. (2005) emphasize the importance of determining total stellar ages in order to associate any WD with thick disk or halo. Currently, there are only a handful of probable field halo WDs known: WD 0346+246 (Hambly et al. 1997), SDSS J1102+4113 (Hall et al. 2008), J2137+1050, and J2145+1106 with $T_{\text{eff}} \approx 3800$ K (Kilic et al. 2010).

Deep, wide-field surveys like Pan-STARRS1 provide the best opportunity to identify significant numbers of thick disk and halo WDs. The combination of astrometry from the SDSS and the Pan-STARRS1 3π survey can be used to identify high proper motion targets in the $>10,000$ square degree overlap area. Better yet, the combination of depth (complete to $r_{\text{P1}} \sim 24.5$), temporal coverage (50–200 epochs over two years), colors (5 bands ranging from 400 nm to 1.1 microns) and photometric and astrometric precision over the 80 square degrees spanned by the Pan-STARRS1 Medium-Deep fields is an excellent data set for discovering faint WD stars.

Here, we present a suite of 47 candidate WDs selected from a combination of proper motion and colors from the Pan-STARRS1 (PS1) Medium-Deep Survey. The remainder of the introduction summarizes the Pan-STARRS1 survey system. The observations we used are described in Section 2. Data processing is outlined in Section 3, and results are shown in Section 4, followed by our conclusions in Section 5.

1.1. The Pan-STARRS1 Telescope and the Gigapixel Imager

The Pan-STARRS1 system is a high-etendue wide-field imaging system, designed for dedicated survey observations. The system is installed on the peak of Haleakala on the island of Maui in the Hawaiian island chain. Routine observations are conducted remotely from the Waiakoa Laboratory in Pukalani. We provide below a terse summary of the Pan-STARRS1 survey instrumentation. A more complete description of the Pan-STARRS1 system, both hardware and software, is provided by Kaiser *et al.* (2010). The survey philosophy and execution strategy are described in Chambers *et al.* (in prep).

The Pan-STARRS1 optical train (Hodapp *et al.* 2004) uses a 1.8 meter diameter $f/4.4$ primary mirror, and a 0.9 m secondary. The resulting converging beam then passes through two refractive correctors, an interference filter with a clear aperture diameter of 496mm, and a final refractive corrector that is the dewar window.

The Pan-STARRS1 imager (Tonry *et al.* 2008) comprises a total of 60 4800×4800 pixel detectors, with $10 \mu\text{m}$ pixels that subtend 0.258 arcsec. The diameter of the field illuminated by the optical system is 3.3 degrees. The detectors are back-illuminated CCDs manufactured by Lincoln Laboratory. The detectors are read out using a StarGrasp CCD controller (Onaka *et al.* 2008), with a readout time of 7 seconds for a full unbinned image.

The Pan-STARRS1 passbands are designated as g_{P1} , r_{P1} , i_{P1} , z_{P1} and y_{P1} in order to clearly distinguish PS1 from other photometric systems. Photometry in the PS1 system is on the AB magnitude system ((Fukugita *et al.* 1996)).

Images obtained by the Pan-STARRS1 system are processed through the Image Processing Pipeline (IPP), on a computer cluster at the Maui High Performance Computer Center. The pipeline runs the images through a succession of stages, including flat-fielding (“de-trending”), a flux-conserving warping to a sky-based image plane, masking and artifact removal, and object detection and photometry (Magnier 2006). The IPP also performs image subtraction to allow for the prompt detection of variables and transient phenomena. For the results presented here, the flat-fielded and warped Medium-Deep images were processed through a custom stacking and calibration process, as described in section 3. These data

are collected with many dithers, permitting an outlier rejection strategy that exempts them from the “Magic” satellite streak masking software.

1.2. The Pan-STARRS1 Photometric System

The Pan-STARRS1 observations are obtained through a set of five broadband filters, which we have designated as g_{P1} , r_{P1} , i_{P1} , z_{P1} , and y_{P1} . Under certain circumstances Pan-STARRS1 observations are obtained with a sixth, “wide” filter designated as w_{P1} that essentially spans g_{P1} , r_{P1} , and i_{P1} . Although the filter system for Pan-STARRS1 has much in common with that used in previous surveys, such as SDSS (York et al. 2000), there are important differences. The g_{P1} filter extends 20 nm redward of g_{SDSS} , paying the price of 5577Å sky emission for greater sensitivity and lower systematics for photometric redshifts, and the z_{P1} filter is cut off at 930 nm, giving it a different response than the detector response defined z_{SDSS} . SDSS has no corresponding y_{P1} filter. We stress that, like SDSS, Pan-STARRS1 uses the AB photometric system and there is no arbitrariness in the definition, only in how accurately we know the bandpasses.

The details of the photometric calibration and the Pan-STARRS1 zeropoint scale will be presented in a subsequent publication (Tonry *et al.* in prep), and (Magnier *et al.* in prep) will provide the application to a consistent photometric catalog over the 3/4 sky observed by Pan-STARRS1. We briefly describe the methodology used for the photometry presented in this paper.

We have carried out extensive, in-situ measurements of the full transmission of the Pan-STARRS1 system (Stubbs et al. 2010), as well as knowing the filter, lens, and mirror characteristics from vendor’s measurements, and we have found these to be consistent. Provisional response functions (including 1.2 airmasses of atmosphere) are available at the project’s web site¹.

Integrating the Pan-STARRS1 SDSS, and Johnson/Kron-Cousins bandpasses against spectrophotometry of 273 stars with a wide range of temperature and surface gravity gives us a means of transforming SDSS colors to the Pan-STARRS1 system for the stellar locus. Table 1 relates the Pan-STARRS1 color to a corresponding SDSS color: $C_{P1} = A + B \times C_{SDSS}$, valid over a certain range in C_{SDSS} . Since both systems are AB the constant A is negligible, and the relative redness of g_{P1} and blueness of z_{P1} relative to SDSS are reflected in $B < 1$. The term for y_{P1} is purely a stellar locus extrapolation off of the SDSS system and should

¹http://svn.pan-starrs.ifa.hawaii.edu/trac/ipp/wiki/PS1_Photometric_System

be used with caution.

Table 1: Pan-STARRS1 – SDSS stellar color transformations

C_{P1}	C_{SDSS}	A	B	rms	Color range
$(g - r)_{\text{P1}}$	$(g - r)_{\text{SDSS}}$	-0.016	0.865	0.012	-0.6 – 1.6
$(r - i)_{\text{P1}}$	$(r - i)_{\text{SDSS}}$	-0.002	1.018	0.004	-0.5 – 1.0
$(i - z)_{\text{P1}}$	$(i - z)_{\text{SDSS}}$	+0.001	0.837	0.008	-0.5 – 1.2
$(z - y)_{\text{P1}}$	$(i - z)_{\text{SDSS}}$	-0.004	0.400	0.022	-0.2 – 1.2

Note. — The columns contain the Pan-STARRS1 color, the SDSS color, the offset A [mag], the color coefficient B , the rms scatter [mag] between the synthetic spectrophotometry in the Pan-STARRS1 system and the color-transformed SDSS-band synthetic photometry, for the 273 sources used, and the color range (SDSS) [mag] over which this RMS holds.

While the catalog of Magnier *et al.* (in prep) will use Pan-STARRS1 as a photometric instrument to link observations to fundamental standards such as Vega or BD+17 4708, the photometry presented here is based on SDSS DR7. Each Medium-Deep field observation in a filter is brought into relative calibration with every other observation, and then overlap with SDSS stars whose magnitudes have been transformed into the Pan-STARRS1 system provides a single zeropoint for all. We finally use the stellar locus of Covey *et al.* (2007) transformed to the Pan-STARRS1 system to provide cross-filter zero-point tweaks and create the most consistent colors possible. The procedure is described in detail below, but it is essential to emphasize that the photometry here is on the Pan-STARRS1 system, not on the SDSS system, although SDSS is the basis for zeropoints and colors. Like SDSS, the Pan-STARRS1 photometry includes 1.2 airmasses of atmospheric attenuation as a factor in the bandpasses, although the magnitudes are corrected to the top of the atmosphere. No correction is made for galactic extinction.

2. OBSERVATIONS

In addition to covering the entire sky at $\delta > -30$ deg, the Pan-STARRS1 survey has obtained multi-epoch images in the g_{P1} , r_{P1} , i_{P1} , z_{P1} and y_{P1} bands of the fields listed in Table 2, the Medium-Deep fields. MD00 is a field centered on M31 with a filter choice and cadence designed to detect microlensing. This paper uses only the images and photometry from the 1635 Pan-STARRS1 Medium-Deep Field survey observations acquired between Apr

2009 and Apr 2011. There are some 350 observations that missed IPP processing in time for inclusion.

Table 2: Pan-STARRS1 Medium-Deep Field Centers.

Field	RA (J2000)	Dec (J2000)
MD00	10.675	41.267
MD01	35.875	−4.250
MD02	53.100	−27.800
MD03	130.592	44.317
MD04	150.000	2.200
MD05	161.917	58.083
MD06	185.000	47.117
MD07	213.704	53.083
MD08	242.787	54.950
MD09	334.188	0.283
MD10	352.312	−0.433
MD11	270.000	66.561

Observations of the Medium-Deep fields occur each night, cycling through the various Pan-STARRS1 filters, during that portion of the year that the fields are accessible at less than 1.3 airmasses. A nightly “observation” in a given filter consists of 8 dithered “exposures”, with a typical cadence as shown in Table 3. Our basic units of observation are these “nightly-stacks” and the “stack-stack” of all nightly-stacks, although there is information available on the timescales of individual exposures, and for other programs we assemble custom stacks of nightly-stacks.

Table 3: Pan-STARRS1 Medium-Deep Survey, typical cadence. Observations taken 3 nights on either side of full moon are done only in the y_{P1} band.

Night	Filter	Exposure Time
1	g_{P1} & r_{P1}	8×113 s each
2	i_{P1}	8×240 s
3	z_{P1}	8×240 s
repeats...
FM \pm 3	y_{P1}	8×240 s

Table 4 provides basic information about each field and filter, including the number of nightly-stacks available, the total exposure time, the PSF FWHM calculated by DoPhot on the stack-stack, the median PSF of the various nightly-stacks estimated by IPP, and the $5\text{-}\sigma$ limiting magnitude for point sources. This limiting magnitude was calculated by creating two stacks from interleaved halves of all the nightly-stacks, comparing DoPhot photometry between them, estimating the magnitude where the RMS difference is 0.2 mag, and from that deriving the magnitude where the sum would have RMS uncertainty 0.2 mag. We can relate this limiting magnitude to the RMS magnitude per $0.2''$ pixel of the background and the PSF FWHM, w , (in arcsec). This RMS background in turn for each filter depends on the exposure time, t , and a constant that folds together the mean system throughput, sky background, and extinction.

$$\text{RMS} = (24.3, 24.1, 23.7, 23.1, 22.0) + 1.25 \log(t) \quad (1)$$

$$m_{lim} = \text{RMS} - 5.4 - 2.5 \log(w), \quad (2)$$

where the sequence in parentheses corresponds to $g_{P1}, r_{P1}, i_{P1}, z_{P1}, y_{P1}$. The core-skirt nature of the PSF in the stack-stack (discussed in more detail below) implies that these $5\text{-}\sigma$ limits degrade slowly for larger apertures (e.g. for galaxy photometry).

3. DATA PROCESSING

3.1. Individual Image Processing

The Pan-STARRS1 IPP system performs flatfielding on each of the images, using white light flatfield images from a dome screen, in combination with an illumination correction obtained by rastering sources across the field of view. Bad pixel masks are applied, and carried forward for use in the stacking stage. After determining an initial astrometric solution, the flat-fielded images are then warped onto a tangent plane of the sky, using a flux conserving algorithm. The plate scale for the warped images is 0.200 arcsec/pixel. The IPP removes the sky level from the images, but at this point makes no attempt to provide a consistent flux scale. Images obtained through clouds are included in the processing chain. We adjust the flux scale of each image at the level of a Pan-STARRS1 “skycell”, which subtends 20 arcminutes on the sky. There is no evidence for residual spatial structure in the attenuation from clouds in the resulting Medium-Deep field nightly stacks, each combining 8 images of integration time over 100 seconds.

Table 4: Pan-STARRS1 MDF Statistics, Apr 2009–Apr 2011.

Field	Filter	N	$\log t$	PSF	$\langle w \rangle$	m_{lim}	Field	Filter	N	$\log t$	PSF	$\langle w \rangle$	m_{lim}
MD01	g_{P1}	42	4.7	1.25	1.55	24.5	MD06	g_{P1}	38	4.6	1.25	1.56	24.4
MD01	r_{P1}	42	4.7	1.15	1.35	24.4	MD06	r_{P1}	39	4.6	1.18	1.45	24.2
MD01	i_{P1}	41	4.9	1.05	1.27	24.4	MD06	i_{P1}	41	4.9	1.14	1.39	24.3
MD01	z_{P1}	41	4.9	1.03	1.24	23.9	MD06	z_{P1}	38	4.9	1.05	1.30	23.7
MD01	y_{P1}	21	4.6	0.95	1.17	22.4	MD06	y_{P1}	24	4.7	1.00	1.25	22.4
MD02	g_{P1}	30	4.5	1.31	1.79	24.2	MD07	g_{P1}	36	4.5	1.23	1.68	24.3
MD02	r_{P1}	29	4.5	1.20	1.74	24.1	MD07	r_{P1}	39	4.5	1.13	1.46	24.2
MD02	i_{P1}	30	4.8	1.11	1.50	24.2	MD07	i_{P1}	39	4.9	1.14	1.44	24.2
MD02	z_{P1}	33	4.8	1.06	1.30	23.6	MD07	z_{P1}	43	4.9	1.08	1.37	23.7
MD02	y_{P1}	16	4.5	1.14	1.42	22.1	MD07	y_{P1}	30	4.8	1.01	1.28	22.5
MD03	g_{P1}	38	4.6	1.18	1.44	24.5	MD08	g_{P1}	38	4.5	1.27	1.68	24.3
MD03	r_{P1}	37	4.6	1.09	1.28	24.4	MD08	r_{P1}	38	4.5	1.14	1.47	24.2
MD03	i_{P1}	41	4.9	1.06	1.31	24.4	MD08	i_{P1}	33	4.8	1.07	1.34	24.2
MD03	z_{P1}	42	5.0	1.03	1.27	23.9	MD08	z_{P1}	40	4.9	1.09	1.39	23.7
MD03	y_{P1}	20	4.6	1.00	1.36	22.4	MD08	y_{P1}	32	4.9	0.98	1.27	22.7
MD04	g_{P1}	35	4.6	1.17	1.52	24.5	MD09	g_{P1}	34	4.5	1.26	1.55	24.3
MD04	r_{P1}	37	4.6	1.09	1.46	24.3	MD09	r_{P1}	33	4.5	1.15	1.42	24.1
MD04	i_{P1}	35	4.9	1.07	1.35	24.3	MD09	i_{P1}	34	4.8	1.02	1.36	24.3
MD04	z_{P1}	28	4.8	1.03	1.32	23.6	MD09	z_{P1}	34	4.8	1.02	1.26	23.7
MD04	y_{P1}	8	4.3	1.03	1.21	22.0	MD09	y_{P1}	12	4.3	0.94	1.12	22.0
MD05	g_{P1}	42	4.6	1.24	1.58	24.4	MD10	g_{P1}	30	4.5	1.26	1.60	24.2
MD05	r_{P1}	40	4.6	1.17	1.46	24.3	MD10	r_{P1}	33	4.5	1.18	1.53	24.2
MD05	i_{P1}	34	4.8	1.06	1.44	24.3	MD10	i_{P1}	30	4.8	1.01	1.31	24.2
MD05	z_{P1}	27	4.8	0.99	1.27	23.6	MD10	z_{P1}	28	4.8	1.03	1.24	23.6
MD05	y_{P1}	17	4.6	1.02	1.33	22.3	MD10	y_{P1}	11	4.4	0.96	1.22	22.2
MD11	g_{P1}	1	3.0	1.17	1.45	22.4	MD00	g_{P1}	0
MD11	r_{P1}	1	3.0	1.12	1.30	22.3	MD00	r_{P1}	101	4.9	1.03	1.30	24.8
MD11	i_{P1}	3	3.8	1.13	1.47	22.9	MD00	i_{P1}	66	4.6	0.96	1.25	24.0
MD11	z_{P1}	4	3.9	1.34	1.81	22.2	MD00	z_{P1}	0
MD11	y_{P1}	5	4.0	0.96	1.21	21.6	MD00	y_{P1}	0

Note. — N is the number of nights of observation, $\log t$ is the \log_{10} of the net exposure time in sec, “ PSF ” is the DoPhot FWHM of the *core-skirt* PSF in the stack-stacks (in arcsec), $\langle w \rangle$ is the median IPP FWHM of the observations (in arcsec), and m_{lim} is the 5σ detection limit for point sources.

3.2. Exposure combination into stacks

The images obtained from a single night in each band were typically obtained with small dithers in boresight and at a diversity of rotator angles. The stack of 8 images per band per night were then assembled into a “nightly stack”, using a variance-weighted combination of individual frames, with outlier rejection. These nightly-stacked images are considered to be that night’s image in the appropriate band. This stacking process successfully suppresses cosmic ray artifacts, masking losses, and any sources that move a distance larger than the PSF during the ~ 30 minute observation interval.

Nightly-stacks are combined into “stack-stacks” by weighting each by inverse variance times inverse PSF area. We find that this is nearly optimal for point source detection. In principle we might do slightly better by convolution with PSF, but in practice the covariance between warped pixels is such as to make the improvement negligible. The resulting PSF of this stack-stack has a relatively sharp core and substantial skirt, of course, but we do not attempt to deconvolve the skirt into a more compact PSF, even though it would be a relatively robust operation. Instead, we always strive to match PSF models to the data, or include skirt deconvolution as part of the normal kernel convolution required when image subtracting the stack-stack from a nightly-stack.

3.3. Photometric and astrometric calibration

In the interim, before the Pan-STARRS1 photometric catalog of the sky is released, we must resort to a somewhat involved procedure to bring all observations to a common and accurate zeropoint. In brief, these steps are applied to each set of observations of each Medium-Deep field, every 20 arcminute skycell of each field (about 70 per field), and each filter:

1. Obtain instrumental magnitudes (fluxes) for all stars in all nightly-stacks using DoPhot (Schechter et al. 1993).
2. By comparison of stellar instrumental magnitudes between all $N(N-1)/2$ pairs of observations (Tonry *et al.* in prep), obtain photometric and astrometric offsets for each skycell of each nightly-stack (with indeterminate zeropoint). All instrumental magnitudes are corrected to an aperture magnitude within a 6 arcsec box.
3. Combine all nightly-stacks into a stack-stack using inverse variance times inverse PSF area weighting.

4. Obtain instrumental magnitudes for all stars in each stack-stack.
5. Assemble a weighted combination of three estimates of photometric zeropoint by comparing a) SDSS stars converted to the Pan-STARRS1 system (or its extension to MD01 and MD02 using relative photometry from Pan-STARRS), b) z_{P1} derived from 2MASS magnitudes and stellar locus conversions, and c) skycell-to-skycell relative zeropoints founded on the flattening performed by the IPP with the instrumental magnitudes of the stack-stack.
6. Create an “object catalog” from the union over all filters for each skycell; perform forced-position photometry on each stack-stack for each object in the catalog.
7. Compare four colors for all stellar objects in five filters with the standard colors of the stellar locus. This is derived by removing (small for MDS) SFD extinction from each object and matching to the stellar locus (Covey et al. 2007), shifted to the Pan-STARRS1 system. Apply these (very small) offsets to the zeropoints of each filter, assuming zero median. This corrects (High *et al.* 2009) for small residual effects in color-color space, such as atmospheric extinction variations or small color terms between skycells.

This has the following features.

- All nightly-stacks and stack-stacks should have very consistent photometry, limited by DoPhot’s ability to match the PSF and the size of the aperture box.
- Use of the flattening constraint should prevent skycell to skycell jumps in zeropoint.
- The skycell by skycell tie to a standard stellar locus should make colors more accurate than absolute zeropoints.
- The absolute astrometry is founded on the 2MASS coordinate system that IPP currently uses to create the warps, but does remove small offsets (typically less than ~ 50 mas) between nightly-stacks that have occurred as IPP evolves. This ensures that the relative astrometry for proper motions is as accurate as we can currently make it.

Although this will eventually be superseded by the Pan-STARRS1 photometric and astrometric system, we believe that this procedure has satisfactory accuracy for our purposes.

Figure 1 shows the stellar locus of 500,000 stars from the ten Medium-Deep fields. The width of the locus in $(r - i)_{P1}$ at $(g - r)_{P1} = 0.6$ is 0.04 mag, consistent with the estimated uncertainties in the photometry added in quadrature to 0.02 mag, and constraining any failure to bring skycells and Medium-Deep field photometry into color agreement to ~ 0.02 mag.

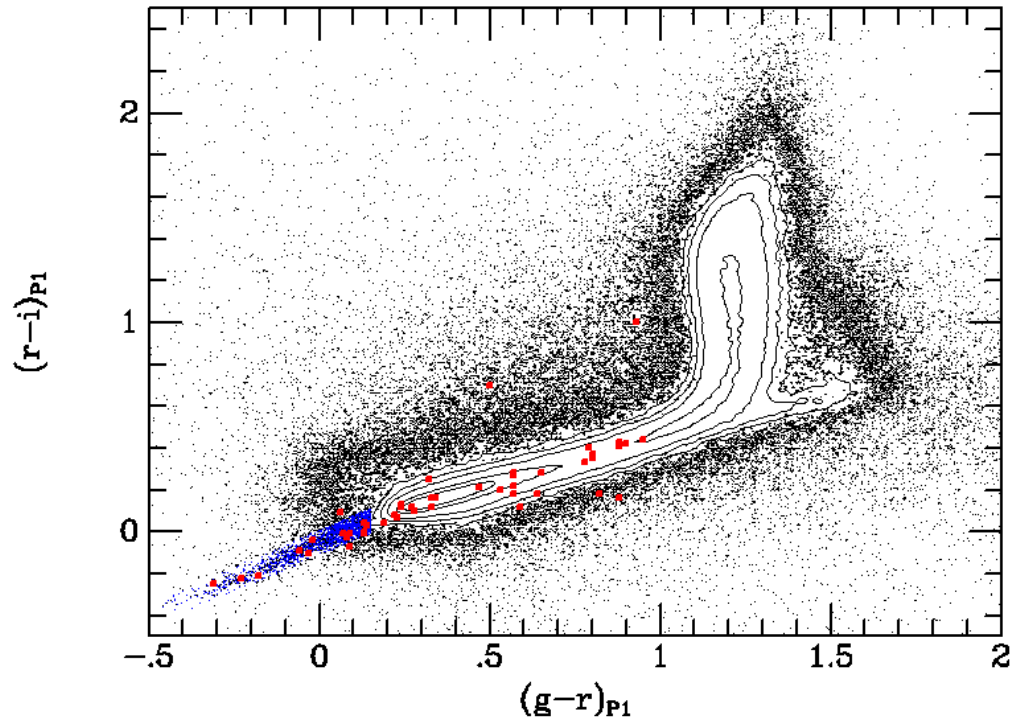


Fig. 1.— Pan-STARRS1 Medium-Deep Field stellar locus of 500,000 stars in 10 MDFs. The 47 Pan-STARRS1 WD candidates are shown as square, red points. The blue extension of the stellar locus (~ 1800 stars shown in blue) are likely hot WD stars, but luminosity inferred from proper motion is a prerequisite to identify cool WDs that overlap the stellar locus.

3.4. Proper motion determination

There are some 10 million objects in the 10 MD fields for which we have 50–200 observations, spread over 2 years and the five filters. We have searched these for evidence of proper motion. The RMS astrometric residuals for sufficiently bright objects (photometric precision of <0.05 mag) is 25–40 mas, per observation. For each object we assemble all the detections and fit the positions for a proper motion. Objects with $r_{P1} < 22$ typically yield an answer with uncertainty of ~ 10 mas/yr; fainter objects can be measured with correspondingly greater uncertainty. For brighter objects we can find SDSS or even USNO-B counterparts, but many are too faint.

There are some 60,000 objects that appear to have a 3σ proper motion in this 2 year data. We further cut this by demanding a 6σ proper motion significance, and we also augment the skycell alignment described above by a local astrometric bias correction. This consists of finding all objects within 0.03 deg of each candidate proper motion that themselves are more significant than 1.5σ (typically ~ 40 objects), assembling a median motion and quartile-derived RMS, subtracting this median motion from the candidate proper motion and adding the uncertainty in quadrature to the uncertainty of the candidate's. This has the effect of reducing the systematic error although increasing the uncertainty, and decreasing the number that still meet the 6σ criterion. There are about 1,000 objects that fulfill this bias-corrected, 6σ cut.

There are a number of improvements we anticipate in the near future.

- Once Pan-STARRS1 moves to its own astrometric system instead of 2MASS, the need for this skycell adjustment and local bias correction should disappear, and we should see significantly tighter residuals for bright enough objects.
- To date we have worked only with nightly-stacks, but of course it is possible to combine observations to achieve better astrometric precision for faint objects at the expense of fewer epochs.
- The present Pan-STARRS1 mission is slated to continue for at least two more years, doubling or tripling the temporal baseline (there were far fewer observations in 2009 than in 2010).

Although the colors of the majority of the 10 million objects lie off of the stellar locus, these 1,000 objects (and 60,000 3σ objects) lie gratifyingly close to the stellar locus; extremely few galaxies leak past the proper motion filter.

Comparisons with the SIMBAD database of known proper motions show excellent agreement for those objects faint enough not to be saturated for Pan-STARRS1 and bright enough to appear in SIMBAD. At $r_{P1} \sim 15$ only the poor seeing Pan-STARRS1 observations are unsaturated, Pan-STARRS1 achieves its best accuracy for objects in the range of $17 < r_{P1} < 21$, and without nightly-stack combination Pan-STARRS1 loses accuracy to photon statistics fainter than $r_{P1} > 22$.

3.5. Parallax fits

Joint fits for parallax and proper motion over the baseline of Pan-STARRS1 observations did not turn up any highly significant parallax: the median uncertainty is 10 mas and the median parallax is 4 mas. There were three detections of parallax at 2.5σ at 13, 27, and 29 mas, but the covariance with proper motion make these very insecure measurements. (Of course there are many stars in the MD fields closer than 30 pc, but they are all too bright and saturated.) We anticipate much better performance when we have the Pan-STARRS1 astrometric grid, perhaps uncertainties as small as 3 mas for bright objects with $17 < r_{P1} < 21$. Of course, the extended time baseline over the course of the Pan-STARRS1 project will also help improve the proper motion and parallax measurements.

4. RESULTS

4.1. Selection of WDs by Reduced Proper Motion

The “reduced proper motion” (RPM) is defined as $H = m + 5 \log \mu + 5 = M + 5 \log v_{tan} - 3.379$, where μ is measured in arcsec/yr and v_{tan} in km/s, and is therefore a proxy for absolute magnitude for a given transverse velocity. With accurate photometry and astrometry, these diagrams can reveal a very clean separation of stars into main sequence, subdwarfs, and WDs. For example, the contamination rate of the WD locus by subdwarfs is only 1-2% for the SDSS + USNO-B RPM diagram (Kilic et al. 2006). The H_{gP1} vs. $(g - r)_{P1}$ and H_{rP1} vs $(r - i)_{P1}$ RPM diagrams for our 1,000 proper motions are presented in Figure 2. That the gap between subdwarfs and WDs is so clearly visible is a testament to the high accuracy of the Pan-STARRS1 photometry and proper motions at this relatively stringent selection criterion.

We use these RPM diagrams to identify 47 WD candidates. Astrometric and photometric data for these objects are given in Table 5 and 6, respectively. About half of our sample has proper motion measurements available in the literature (Munn et al. 2004;

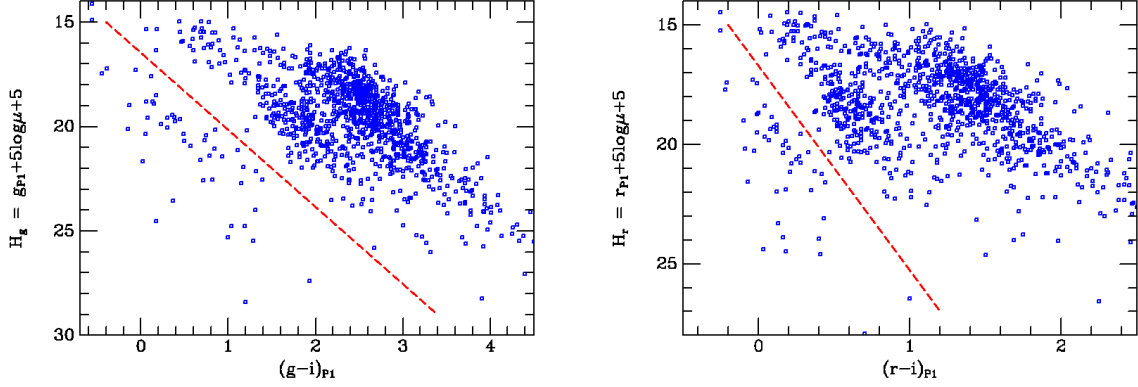


Fig. 2.— Pan-STARRS1 Medium Deep Field Proper Motion Diagrams. Left panel is in g_{P1} i_{P1} space, and the right panel is in r_{P1} , i_{P1} space. The large clump on the right is main sequence stars; the middle clump that separates well in $(r - i)_{P1}$ are subdwarfs, and the blue, faint objects on the left are candidate WD stars.

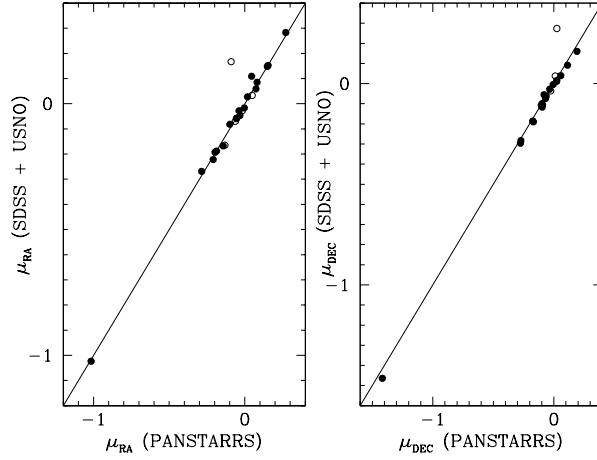


Fig. 3.— Pan-STARRS1 (this work) versus SDSS+USNO-B or LSPM (Munn et al. 2004; Lépine & Shara 2005) proper motion measurements for 24 WD candidates. Objects with unreliable SDSS+USNO-B proper motions (detected in <5 epochs) are shown as open circles.

Lépine & Shara 2005). Figure 3 shows a comparison of our proper motion measurements and the literature values. Open circles mark the objects with unreliable proper motions from the SDSS + USNO-B. Ignoring those, there is an overall agreement between our proper motion measurements and the literature values.

Table 5. Pan-STARRS1 MDF White Dwarf Candidates, Astrometric Data. The columns present Object ID designations, RA and Dec (J2000) in decimal degrees (for epoch 2010.5) the number of valid astrometric observations per star, the measured proper motions in RA and Dec (in mas per year), their associated uncertainties, the fitted parallax and its uncertainty, in mas. (We do not regard any of the parallax values to be significant.)

OBJID	RA(J2000)	Dec(J2000)	N_{pts}	μRA	$\sigma_{\mu RA}$	μDec	$\sigma_{\mu Dec}$	π	σ_{π}
PSO J035.1219–04.4538	35.12198	-4.45385	120	49	15	-106	16	23	10
PSO J036.1807–02.7150*	36.18072	-2.71503	85	392	19	37	21	4	16
PSO J036.1820–02.7157*	36.18203	-2.71578	80	383	21	53	24	2	16
PSO J053.8940–27.1420	53.89408	-27.14205	68	49	31	-343	35	11	19
PSO J053.9285–27.4034	53.92850	-27.40348	107	51	18	102	16	29	10
PSO J128.8195+44.7108	128.81959	44.71086	131	12	13	-120	13	12	10
PSO J128.9494+44.4259	128.94944	44.42598	172	-3	7	-64	7	8	6
PSO J130.1413+43.5130	130.14136	43.51305	138	-17	10	-70	10	-8	7
PSO J130.3780+44.1562	130.37809	44.15620	157	71	9	-53	9	-6	8
PSO J130.5828+43.8370	130.58286	43.83708	158	-37	9	-52	9	-15	7
PSO J131.0677+45.8815	131.06776	45.88157	25	51	53	-253	41	-36	34
PSO J131.2406+45.6086	131.24064	45.60864	175	-54	10	-175	9	11	6
PSO J132.0255+43.9883	132.02558	43.98836	145	-86	12	-10	11	-12	9
PSO J132.2560+44.6595	132.25604	44.65954	177	-197	13	-96	12	12	6
PSO J148.6936+01.4568	148.69365	1.45680	54	149	19	-272	20	0	23
PSO J148.9818+03.1285	148.98181	3.12853	51	-14	39	-249	36	-28	48
PSO J149.3101+02.6967	149.31014	2.69677	136	-187	8	-104	8	14	10
PSO J149.3311+03.1446	149.33117	3.14463	120	45	10	-94	9	4	10
PSO J149.7106+01.7900	149.71066	1.79004	142	74	11	-6	15	13	9
PSO J149.7616+01.6465	149.76161	1.64656	140	18	9	-69	12	1	9
PSO J149.8925+02.9603	149.89256	2.96030	141	-59	12	-96	10	27	9
PSO J150.1696+03.6030	150.16966	3.60309	115	9	11	-90	11	-7	13
PSO J150.8329+02.1407	150.83292	2.14079	117	-90	12	25	11	1	15
PSO J151.3094+02.9046	151.30944	2.90467	114	-692	14	18	14	1	14
PSO J159.5163+57.6086	159.51636	57.60867	110	-10	12	-259	12	4	12
PSO J160.5173+58.5631	160.51739	58.56312	148	-99	14	-81	12	-1	8
PSO J160.6208+59.0860	160.62083	59.08602	44	-438	66	-49	65	-23	59
PSO J161.4917+59.0766	161.49173	59.07662	98	-1016	13	-1417	12	22	11
PSO J161.8956+59.2131	161.89562	59.21314	156	-32	14	-169	25	-8	7
PSO J162.2873+57.7484	162.28730	57.74848	23	-60	84	520	84	133	70
PSO J164.1738+57.2466	164.17384	57.24660	141	-13	12	-119	20	19	8

Table 5—Continued

OBJID	RA(J2000)	Dec(J2000)	N_{pts}	μRA	$\sigma_{\mu RA}$	μDec	$\sigma_{\mu Dec}$	π	σ_{π}
PSO J164.1744+58.4375	164.17447	58.43759	140	-132	19	12	15	21	9
PSO J183.8810+46.5039	183.88106	46.50397	178	-285	40	24	15	0	7
PSO J185.6294+46.1184	185.62949	46.11848	155	-63	11	-27	10	11	8
PSO J186.4406+47.1036	186.44063	47.10365	169	-143	13	22	15	-7	7
PSO J213.0478+52.6587	213.04785	52.65875	144	-51	12	72	12	-17	8
PSO J214.3502+52.8743	214.35023	52.87438	172	-55	10	57	20	-12	6
PSO J215.0267+53.3759	215.02672	53.37591	187	98	18	-89	15	13	5
PSO J241.3352+55.9465	241.33522	55.94657	172	-209	11	191	8	-1	5
PSO J242.8803+54.6275	242.88030	54.62755	97	17	16	-98	16	-3	10
PSO J333.8526–00.8187	333.85260	-0.81878	13	616	116	-411	115	11	178
PSO J334.4434–00.3065	334.44341	-0.30654	118	84	13	-58	14	0	15
PSO J334.5518–00.0227	334.55185	-0.02278	125	49	11	-97	11	7	14
PSO J334.7932+00.8453	334.79324	0.84537	136	-102	12	-10	10	18	12
PSO J334.8792+01.0115	334.87925	1.01154	137	271	12	-35	21	17	12
PSO J352.7302+00.4814	352.73028	0.48142	125	154	12	113	13	5	11
PSO J353.2230–00.5556	353.22300	-0.55562	116	65	14	62	15	10	13

Note. — * This appears to be a binary WD pair with a common proper motion.

Table 6. Pan-STARRS1 MDF White Dwarf Candidates, Photometric Data. The columns present Object ID designations, $g_{P1}, r_{P1}, i_{P1}, z_{P1}, y_{P1}$ magnitudes and uncertainties.

OBJID	g_{P1}	$\sigma_{g_{P1}}$	r_{P1}	$\sigma_{r_{P1}}$	i_{P1}	$\sigma_{i_{P1}}$	z_{P1}	$\sigma_{z_{P1}}$	y_{P1}	$\sigma_{y_{P1}}$
PSO J035.1219–04.4538	22.21	0.04	21.26	0.02	20.82	0.02	20.66	0.02	20.64	0.04
PSO J036.1807–02.7150	19.60	0.04	19.01	0.05	18.89	0.05	18.80	0.05	18.70	0.05
PSO J036.1820–02.7157	19.60	0.04	18.96	0.05	18.78	0.05	18.69	0.05	18.62	0.05
PSO J053.8940–27.1420	22.77	0.06	21.89	0.04	21.48	0.03	21.33	0.03	21.28	0.12
PSO J053.9285–27.4034	19.83	0.02	19.89	0.02	19.98	0.03	20.16	0.03	20.35	0.07
PSO J128.8195+44.7108	22.32	0.04	21.52	0.02	21.17	0.02	21.05	0.02	20.98	0.05
PSO J128.9494+44.4259	18.43	0.02	18.66	0.02	18.88	0.02	19.11	0.02	19.24	0.02
PSO J130.1413+43.5130	20.27	0.02	19.99	0.03	19.89	0.02	19.88	0.02	19.91	0.04
PSO J130.3780+44.1562	20.61	0.02	20.28	0.02	20.12	0.02	20.09	0.02	20.04	0.03
PSO J130.5828+43.8370	20.72	0.02	20.45	0.02	20.33	0.03	20.31	0.02	20.33	0.03
PSO J131.0677+45.8815	21.48	0.04	21.24	0.05	21.11	0.05	21.17	0.04	21.20	0.15
PSO J131.2406+45.6086	15.96	0.05	15.98	0.03	16.02	0.03	16.14	0.02	16.27	0.02
PSO J132.0255+43.9883	21.24	0.02	20.92	0.02	20.67	0.02	20.78	0.02	20.90	0.07
PSO J132.2560+44.6595	17.95	0.02	17.62	0.02	17.50	0.02	17.49	0.02	17.52	0.02
PSO J148.6936+01.4568	19.21	0.04	19.12	0.05	19.19	0.05	19.27	0.06	19.24	0.15
PSO J148.9818+03.1285	22.79	0.06	21.91	0.00	21.75	0.00	21.44	0.00	22.30	0.30
PSO J149.3101+02.6967	20.27	0.02	19.47	0.02	19.10	0.02	19.00	0.02	18.95	0.02
PSO J149.3311+03.1446	19.34	0.02	19.10	0.02	18.98	0.02	19.03	0.02	19.01	0.02
PSO J149.7106+01.7900	15.56	0.07	15.87	0.05	16.12	0.02	16.38	0.02	16.52	0.02
PSO J149.7616+01.6465	17.95	0.03	18.13	0.02	18.34	0.02	18.52	0.02	18.68	0.02
PSO J149.8925+02.9603	18.24	0.02	18.11	0.02	18.07	0.02	18.12	0.02	18.21	0.02
PSO J150.1696+03.6030	20.90	0.02	20.56	0.02	20.40	0.02	20.36	0.02	20.42	0.04
PSO J150.8329+02.1407	21.53	0.02	20.96	0.02	20.74	0.02	20.71	0.02	20.81	0.03
PSO J151.3094+02.9046	20.55	0.00	19.76	0.00	19.36	0.00	19.42	0.06	19.18	0.05
PSO J159.5163+57.6086	21.92	0.03	21.04	0.02	20.61	0.02	20.47	0.02	20.41	0.03
PSO J160.5173+58.5631	19.05	0.02	18.96	0.02	18.97	0.02	19.07	0.02	19.16	0.02
PSO J160.6208+59.0860	22.09	0.06	21.27	0.00	21.09	0.07	21.07	0.06	20.70	0.20
PSO J161.4917+59.0766	18.33	0.00	18.19	0.00	18.16	0.00	17.98	0.00	18.14	0.03
PSO J161.8956+59.2131	17.80	0.02	17.83	0.02	17.93	0.02	18.06	0.02	18.19	0.02
PSO J162.2873+57.7484	23.79	0.13	22.86	0.07	21.86	0.04	21.59	0.07	21.43	0.12
PSO J164.1738+57.2466	18.40	0.03	18.27	0.02	18.27	0.02	18.35	0.02	18.51	0.02

Table 6—Continued

OBJID	g_{P1}	$\sigma_{g_{P1}}$	r_{P1}	$\sigma_{r_{P1}}$	i_{P1}	$\sigma_{i_{P1}}$	z_{P1}	$\sigma_{z_{P1}}$	y_{P1}	$\sigma_{y_{P1}}$
PSO J164.1744+58.4375	18.3	0.15	18.24	0.03	18.15	0.04	17.9	0.15	18.09	0.04
PSO J183.8810+46.5039	17.30	0.02	17.08	0.02	17.00	0.02	16.99	0.02	17.05	0.03
PSO J185.6294+46.1184	20.96	0.02	20.39	0.02	20.11	0.02	20.07	0.02	20.09	0.03
PSO J186.4406+47.1036	19.61	0.02	19.04	0.02	18.86	0.02	18.95	0.02	19.05	0.02
PSO J213.0478+52.6587	20.62	0.02	20.54	0.02	20.57	0.02	20.62	0.02	20.70	0.03
PSO J214.3502+52.8743	19.32	0.02	19.25	0.02	19.26	0.02	19.32	0.02	19.41	0.02
PSO J215.0267+53.3759	16.97	0.02	16.84	0.02	16.85	0.02	16.90	0.02	16.94	0.02
PSO J241.3352+55.9465	17.80	0.02	17.57	0.02	17.50	0.02	17.52	0.02	17.56	0.02
PSO J242.8803+54.6275	22.14	0.03	21.24	0.04	20.82	0.02	20.71	0.03	20.60	0.03
PSO J333.8526–00.8187	24.07	0.12	23.57	0.06	22.87	0.05	22.63	0.07	22.56	0.17
PSO J334.4434–00.3065	21.38	0.02	20.73	0.02	20.45	0.02	20.39	0.02	20.48	0.03
PSO J334.5518–00.0227	20.89	0.02	20.32	0.02	20.05	0.02	19.97	0.02	19.95	0.03
PSO J334.7932+00.8453	19.82	0.02	19.63	0.02	19.59	0.02	19.64	0.02	19.68	0.02
PSO J334.8792+01.0115	19.43	0.02	18.96	0.02	18.75	0.02	18.69	0.02	18.73	0.02
PSO J352.7302+00.4814	19.71	0.02	18.93	0.02	18.60	0.02	18.46	0.02	18.43	0.02
PSO J353.2230–00.5556	20.90	0.02	20.37	0.02	20.17	0.02	20.08	0.02	20.08	0.03

4.2. Optical Spectroscopy

Twelve of our candidates have optical spectroscopy available in the literature: all of them are previously known WDs, including 6 DAs, 4 DQs, 1 DC, and 1 DZ. PSO J161.4917+59.0766 (LHS 291) is perhaps the most interesting, with a proper motion of $1.7'' \text{ yr}^{-1}$. The identification of this object in our data demonstrates that the Pan-STARRS1 Medium Deep Field data are able to identify even the fastest moving halo objects.

We obtained spectroscopic observations of six candidates, as summarized in Table 7, with the Hectospec instrument (Fabricant et al. 2005) on the MMT. The objects were selected on the basis of field access and were part of a broader program of Pan-STARRS1 followup spectroscopy. The Hectospec fibers are $1.5''$ in diameter. We operate the spectrograph with the 270 lines/mm grating, providing wavelength coverage 3700–9200 Å and a spectral resolution of 5 Å with a dispersion of 1.2 Å per pixel. The spectra were reduced, including flatfielding and wavelength calibration, by the Telescope Data Center pipeline (Mink et al. 2007), at the Center for Astrophysics. Sky subtraction was performed using the spectra from fibers placed on blank sky regions. Flux calibration was performed using standard star observations from an earlier observing run. Therefore, the absolute flux calibration, as well as the relative continuum shape, of our spectra cannot be trusted. However, this level of resolution is sufficient to identify and separate WDs from metal-poor subdwarfs.

Table 7: Spectroscopic Observations.

PS1 ID	UT Observed	t_{exp} (s)
PSO J162.2873+57.7484	2011-06-08T15:36:46	4500
PSO J164.1738+57.2466	2011-06-09T16:02:41	3600
PSO J183.8810+46.5039	2011-06-13T15:47:10	4800
PSO J213.0478+52.6587	2011-06-06T15:59:53	3600
PSO J215.0267+53.3759	2011-06-06T15:34:21	3600
PSO J242.8803+54.6275	2011-06-06T15:34:23	3600

The resulting spectra are presented in Figure 4. Two of the objects with Hectospec spectra were previously known WDs. PSO J164.1738+57.2466 is a known DZ WD with only Ca H and K absorption visible in its optical spectrum. PSO J215.0267+53.3759 is a known DA WD with Balmer absorption lines. One of the objects observed with Hectospec, PSO J162.2873+57.7484, is too faint for the instrument and conditions, and therefore not included in this figure. The remaining three objects are newly confirmed WDs. PSO J183.8810+46.5039 is a DA WD with a hydrogen atmosphere, whereas the lack of de-

tection of Balmer lines in the relatively warm (see §5.3) DC WD PSO J213.0478+52.6587 indicates that it has a helium-dominated atmosphere. The most interesting of the bunch, PSO J242.8803+54.6275, is a cool DC WD with a featureless spectrum. Even though our spectrum is somewhat noisy, the lack of detection of strong MgH and Na absorption lines in the spectrum of such a red object ($(g-i)_{P1} = 1.32$ mag) confirms the WD classification (see Fig. 5 in Kilic et al. 2006). The spectral classification for these WDs, as well as the previously known WDs, are listed in Table 8. There are 15 candidates with optical spectroscopy available, and all are confirmed as WDs. Hence, our RPM selected sample is likely a clean sample of WDs.

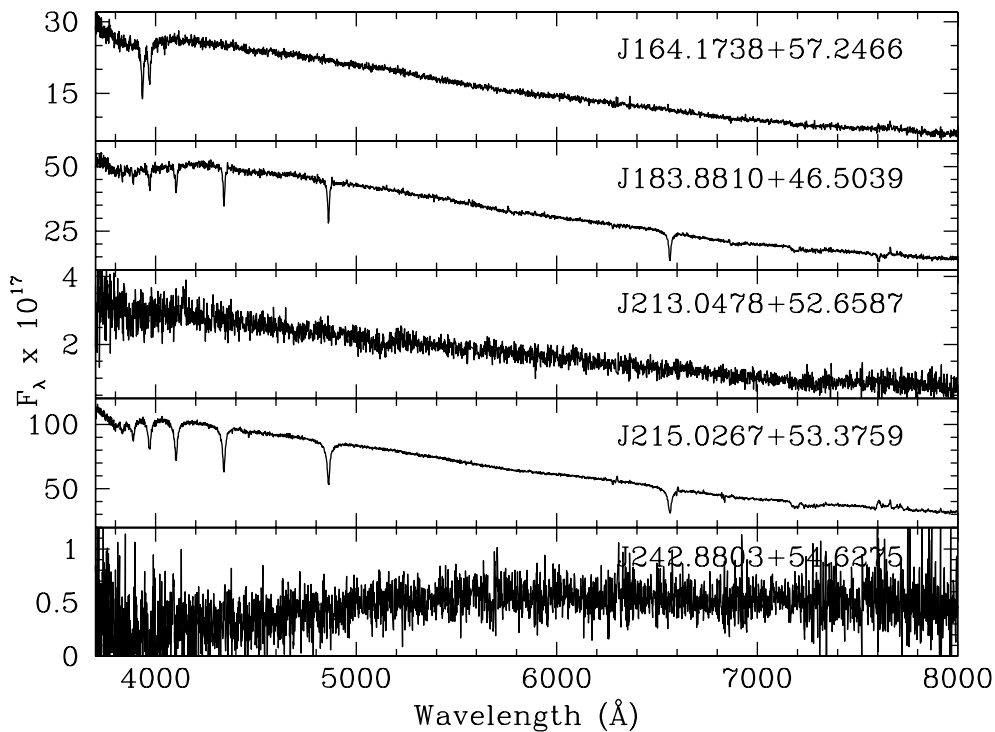


Fig. 4.— MMT Hectospec spectra for five of the objects identified as WD candidates.

4.3. Photometric Distances

Figure 5 shows the optical color-color diagrams for our sample of WDs compared to model predictions from P. Bergeron (2010, private communication). There are two objects, PSO J162.2873+57.7484 and PSO J333.8526-00.8187, with very red (≥ 0.7 mag) $(r-i)_{PS}$

colors. We classify these objects as WD + M dwarf binaries. There are also two other objects, PSO J131.0677+45.8815 and J132.0255+43.9883, with $(u - g)_{SDSS}$ versus $(g - r)_{SDSS}$ colors similar to the known DQ WDs (bottom right panel). These objects may be DQ WDs as well, and optical spectroscopy is needed to see if they show the C_2 swan bands. PSO J148.9818+03.1285 is the only object with a relatively blue $(z - y)_{PS}$ color. Hydrogen-rich cool WDs are expected to show strong flux deficits in the infrared from collision induced absorption due to molecular hydrogen (Bergeron et al. 1995; Hansen 1998). PSO J148.9818+03.1285 may be one such WD. However, the y_{P1} -band measurement for this object has a large error, and therefore, the absorption may not be real. Other than these outliers, the remaining candidates overlap with WD model predictions in various color-color diagrams. Hence, these models can be used to derive temperatures for our targets.

We use all five Pan-STARRS1 magnitudes to fit WD models with hydrogen atmospheres to determine the temperature, absolute magnitude, and distance of each target. Since the Pan-STARRS1 parallax measurements for our targets are inaccurate, we assume a surface gravity of $\log g = 8$ which determines the radius of the star for a given value of temperature. The mass distribution of WDs shows strong peaks at $0.61 \pm 0.1 M_{\odot}$ for DA and $0.67 \pm 0.1 M_{\odot}$ for DB WDs (Tremblay et al. 2011; Bergeron et al. 2011); these ranges imply $\log g = 8 \pm 0.3$. Hence, our assumption of $\log g = 8$ is reasonable.

Cool WD spectral energy distributions are clearly effected by the Ly α red wing opacity in the blue (Kowalski & Saumon 2006). Since these models do not include the Ly α opacity, we use them to analyze only the WDs hotter than 4600 K. For cooler targets, we use the observed colors of cool WDs from Kilic et al. (2009, 2010, analyzed using Kowalski & Saumon (2006) models) as templates to estimate the temperatures of our targets. These templates cover the temperature range 3730-6290 K. Based on the Pan-STARRS1 and the SDSS colors, the temperature estimates from both the models and the templates agree to within 200 K for stars in the temperature range 4600-6000 K.

The photometric spectral energy distributions of six of the coolest objects in our sample are shown in Figure 6. The points with error bars show Pan-STARRS1 photometry and the solid lines show the best-fitting templates. For example, the energy distribution of PSO J035.1219-04.4538 (top left panel) is most similar to the WD SDSS J2222+1221 (Kilic et al. 2009), which has a temperature of 4170 K based on the Kowalski & Saumon (2006) models. Hence, we assign a temperature of 4170 K for PSO J035.1219-04.4538. Given this temperature and assuming $\log g = 8$, we then estimate an absolute magnitude of $M_g = 16.5$ and a distance of 127 pc.

One of the objects in Figure 6, PSO J148.9818+03.1285, may be a WD with a strong y_{P1} flux deficit. If this absorption is real, then the best-fit pure hydrogen atmosphere WD

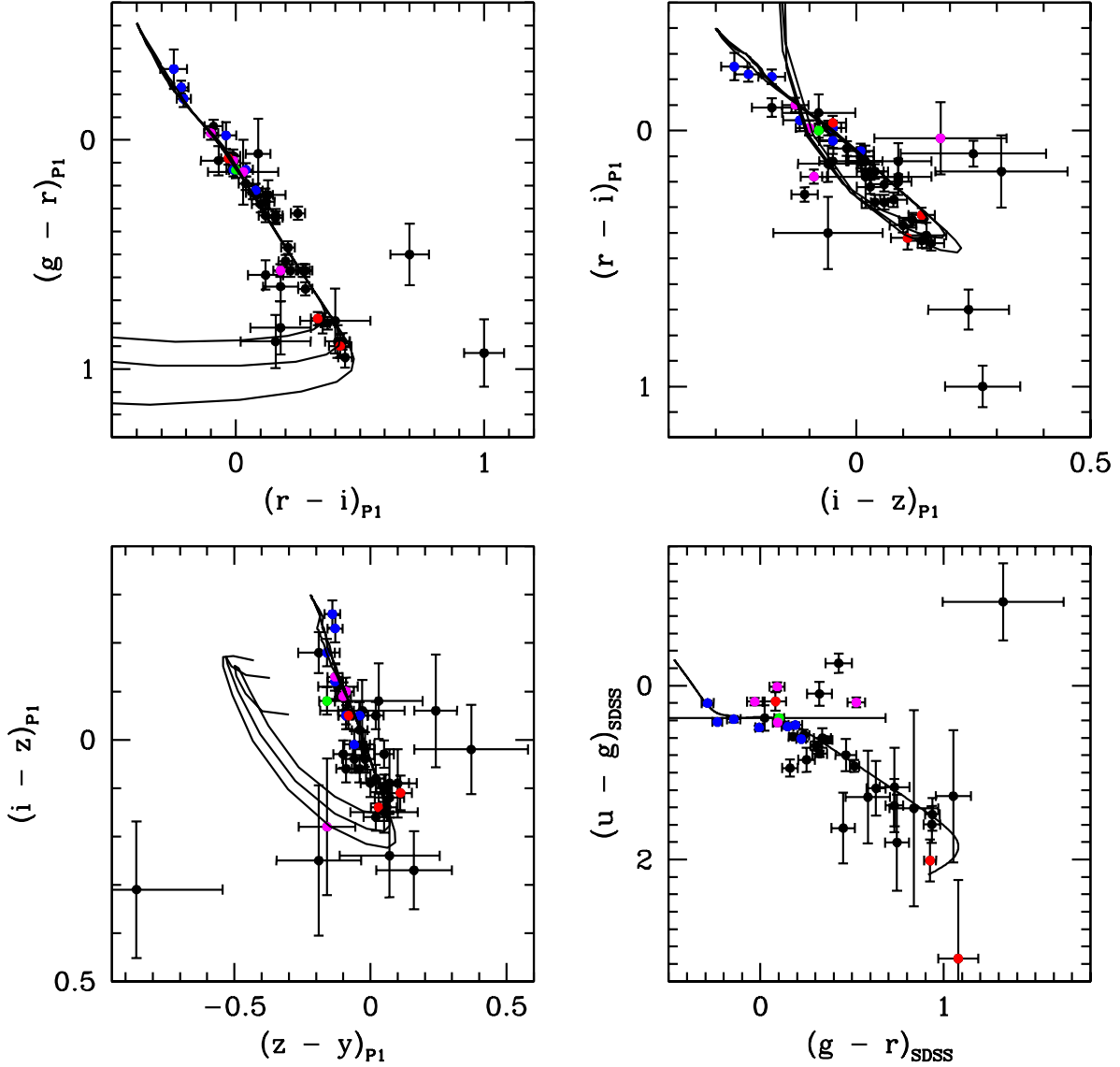


Fig. 5.— Pan-STARRS1 and SDSS (bottom right panel) color-color diagrams for our sample of WD candidates. Spectroscopically confirmed DA (blue), DQ (magenta), DZ (green), and DC (red) WDs are marked. The solid lines show the predicted colors for pure hydrogen atmosphere WDs with $T_{\text{eff}} = 1500 - 110,000$ K and $\log g = 7, 8, \text{ and } 9$ (only the $\log g = 8$ and $T_{\text{eff}} \geq 2000$ K sequence is shown in the bottom right panel).

model would have $T_{\text{eff}} = 3080$ K and a cooling age of 11.1 Gyr. If so, PSO J148.9818+03.1285 would be a very old thick disk or halo WD. However, near-infrared photometry is required to confirm the flux deficit in the infrared and to perform a detailed model atmosphere analysis. Many of the infrared-faint WDs have mixed H/He atmospheres (Kilic et al. 2010), where the effects of the collision induced absorption due to molecular hydrogen become significant at hotter temperatures (>4000 K) compared to the pure hydrogen atmosphere counterparts.

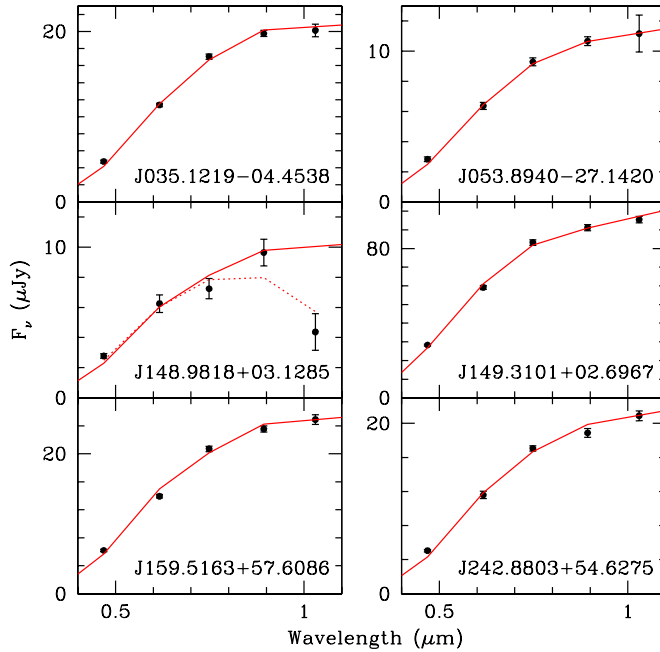


Fig. 6.— Spectral energy distributions of six WDs with $T_{\text{eff}} = 4170 - 4570$ K. Points with error bars show the Pan-STARRS1 photometry. The solid lines show the best-fit cool WD templates. The dotted line shows the predicted model fluxes for a $T_{\text{eff}} = 3080$ K WD.

Table 8 lists the effective temperatures, distances, and tangential velocities for those stars whose position in the RPM diagram and color-color space indicate that they are WDs. The estimated distances and WD cooling ages for our targets range from about 50 pc to 300 pc and 0.2 Gyr to 8.6 Gyr, respectively. Two of the WD candidates, PSO J036.1807–02.7150 and PSO J036.1820–02.7157, form a common proper motion binary system. Our temperature (4900 K and 5100 K) and distance (64 pc and 71 pc) estimates for these two stars agree fairly well, confirming that these two stars are physically associated. The small differences between the temperatures and distances of the two stars can be explained by a small difference in mass.

Table 8. Pan-STARRS1 MDF White Dwarf Candidates, Physical Parameters

OBJID	Type	T_{eff} (K)	d (pc)	V_{tan} (km/s)	Cooling Age (Gyr)
PSO J035.1219–04.4538	...	4170	127	70 ± 19	8.6
PSO J036.1807–02.7150	...	5100	71	133 ± 28	5.2
PSO J036.1820–02.7157	...	4900	64	117 ± 25	6.1
PSO J053.8940–27.1420	...	4280	178	292 ± 71	8.3
PSO J053.9285–27.4034	...	9670	317	171 ± 50	0.7
PSO J128.8195+44.7108	...	4640	177	101 ± 25	7.1
PSO J128.9494+44.4259	DA	13370	249	76 ± 19	0.3
PSO J130.1413+43.5130	...	6150	159	54 ± 15	2.1
PSO J130.3780+44.1562	...	5950	169	71 ± 17	2.3
PSO J130.5828+43.8370	...	6330	205	62 ± 18	2.0
PSO J131.0677+45.8815	...	6540	313	383 ± 125	1.8
PSO J131.2406+45.6086	DA	9110	47	41 ± 9	0.8
PSO J132.0255+43.9883	...	6010	231	95 ± 26	2.2
PSO J132.2560+44.6595	...	6100	53	55 ± 12	2.2
PSO J148.6936+01.4568	...	7950	165	242 ± 53	1.1
PSO J148.9818+03.1285	...	4350	197	233 ± 68	8.0
PSO J149.3101+02.6967	...	4570	67	68 ± 14	7.3
PSO J149.3311+03.1446	...	6480	115	57 ± 14	1.8
PSO J149.7106+01.7900	DA	15670	85	30 ± 10	0.2
PSO J149.7616+01.6465	DA	12160	183	62 ± 18	0.4
PSO J149.8925+02.9603	DA	7890	100	53 ± 13	1.1
PSO J150.1696+03.6030	...	5940	192	82 ± 22	2.4
PSO J150.8329+02.1407	...	5170	179	79 ± 21	4.8
PSO J151.3094+02.9046	...	4570	77	253 ± 51	7.3
PSO J159.5163+57.6086	...	4350	123	151 ± 32	8.0
PSO J160.5173+58.5631	DQ	10080:
PSO J160.6208+59.0860	...	5340	220	459 ± 133	4.0
PSO J161.4917+59.0766	DQ	10110:
PSO J161.8956+59.2131	DQ:	10150:
PSO J162.2873+57.7484	WD+dM?
PSO J164.1738+57.2466	DZ*	7420	99	56 ± 16	1.3

Table 8—Continued

OBJID	Type	T_{eff} (K)	d (pc)	V_{tan} (km/s)	Cooling Age (Gyr)
PSO J164.1744+58.4375	...	6610	79	50 ± 13	1.8
PSO J183.8810+46.5039	DA*	6640	47	64 ± 16	1.7
PSO J185.6294+46.1184	...	5040	128	42 ± 12	5.5
PSO J186.4406+47.1036	DQ	6109
PSO J213.0478+52.6587	DC*	7860	308	129 ± 36	1.1
PSO J214.3502+52.8743	...	7890	170	64 ± 22	1.1
PSO J215.0267+53.3759	DA*	8040	58	36 ± 10	1.1
PSO J241.3352+55.9465	...	6660	60	81 ± 17	1.7
PSO J242.8803+54.6275	DC*	4250	130	61 ± 19	8.4
PSO J333.8526–00.8187	WD+dM?
PSO J334.4434–00.3065	...	4840	138	67 ± 18	6.4
PSO J334.5518–00.0227	...	5000	121	62 ± 15	5.7
PSO J334.7932+00.8453	...	6970	167	81 ± 20	1.5
PSO J334.8792+01.0115	...	5430	78	101 ± 22	3.5
PSO J352.7302+00.4814	DC	5130	67	61 ± 13	5.0
PSO J353.2230–00.5556	...	5210	137	58 ± 18	4.6

Note. — Spectral types for previously known WDs are from Eisenstein et al. (2006), Liebert et al. (2005), Koester & Knist (2006), and Kilic et al. (2006). Asterix (*) designates objects for which we obtained spectra.

Figure 7 shows the distribution of inferred ages and tangential velocities, with the assumption that the distance error is 20%. The coolest WDs in our sample have temperatures around 4200 K. Even though the individual ages for our targets cannot be trusted due to the unknown distances and masses, the average mass for our sample should be about $0.6 M_{\odot}$ and the *average age* for the oldest stars in our sample should be reliable. Adding 1.4 Gyr for the main-sequence lifetime of the $2 M_{\odot}$ solar-metallicity progenitor stars (Marigo et al. 2008) brings the total age to about 10 Gyr, entirely consistent with the oldest disk WDs known (e.g. Table 2 of Leggett et al. 1998) and the Galactic disk age of 8 ± 1.5 Gyr. A few of the oldest targets have large tangential velocities, and therefore they may be halo WDs. However, the velocity errors are also relatively large for those objects. Therefore, all of our targets are consistent with disk membership.

Figure 8 presents finding charts for those new objects that do not reside in the SDSS fields.

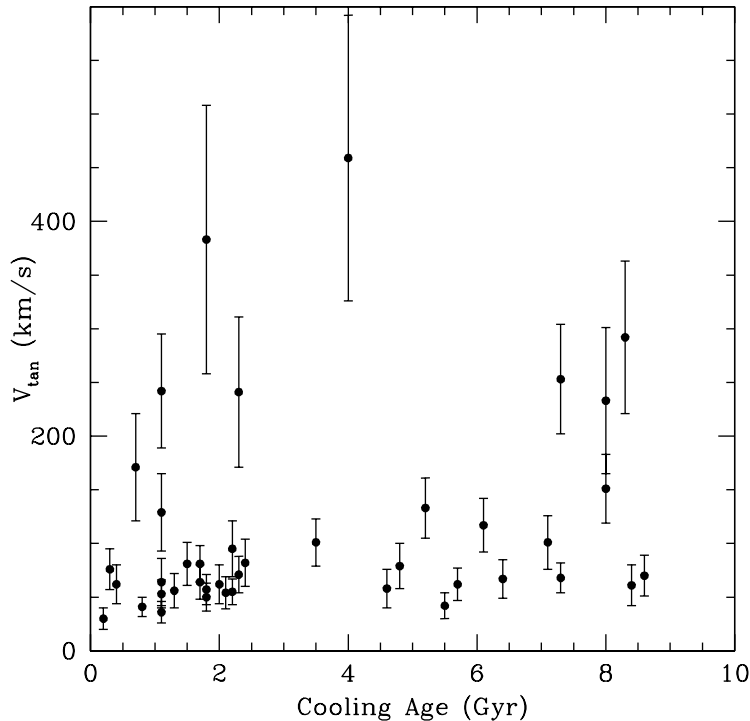


Fig. 7.— Tangential velocities and WD cooling ages for our targets. (The high velocity, young WD presumably have higher mass than $0.6 M_{\odot}$ and their lower luminosity for a given temperature causes us to assign an erroneously high distance and velocity.)

5. DISCUSSION

Deep, wide-field surveys like Pan-STARRS1 provide an unprecedented opportunity for the studies of different stellar populations in the Galaxy. Based on the stellar locus of half a million stars from the ten Medium Deep Fields, we demonstrate that the systematic uncertainty in the Pan-STARRS1 photometric zeropoints is a few percent. In addition, the relatively high-cadence of the Pan-STARRS1 Medium Deep Field observations enable searches for highly variable (e.g. supernovae) and/or moving objects like nearby asteroids or high proper motion stars. Here we take advantage of the first two years of data from the Medium Deep Field observations to select 47 WD candidates using an RPM diagram. We are able to find objects with proper motions as large as $1.7'' \text{ yr}^{-1}$. Hence, we are sensitive to faint halo WDs with large tangential velocities.

A comparison with WD atmosphere models and previously known cool WDs shows that our sample contains WDs down to 4200 K, which corresponds to a main-sequence + WD cooling age of 10 Gyr. A few of the oldest objects in our sample have large tangential velocities that may indicate halo membership. Assuming that the halo is a single burst 12 Gyr old population with 0.4% normalization compared to the disk, Kilic et al. (2010) predict 0.14 halo WDs per square degree down to a limiting magnitude of $V = 21.5$ mag. Our sample of 47 WD candidates is therefore likely to contain a few halo WDs. However, our parallaxes as yet lack adequate accuracy to claim that they are indeed halo WDs. Pan-STARRS1 will continue to observe the Medium Deep Fields over the course of the next two years, and the Pan-STARRS1 astrometric catalog is imminent and will significantly improve the proper motion and parallax precision for these targets.

For this initial project to find WDs in the Pan-STARRS1 data we concentrated on sample purity rather than completeness, and the astrometric bias correction was particularly draconian. We present proper motions to a limit of 60 mas/yr and $g_{P1} \sim 22.5$. Doubling the number of epochs should improve accuracy by $2^{3/2}$ and bring us to measurements of ~ 20 mas/yr with uncertainty of ~ 3 mas/yr. We used the Besançon Galaxy model (Robin et al. 2003) to simulate the stellar populations in the Medium Deep fields. At 20 mas/yr over 70 sq. deg., even without co-adding to improve the nightly-stack detection limit, the model predicts we ought to be able to find some 850 WDs. By co-adding nightly-stacks to reach a limiting magnitude of $g_{P1} \sim 23.5$ this number rises to about 1500. We look forward to being able to probe the halo WD population with such a clean, large sample, and employ them to chart the history of the Milky Way.

Facilities: Pan-STARRS1(GPC), MMT(Hectospec)

Support for this work was provided by National Science Foundation grant AST-1009749. The PS1 Surveys have been made possible through contributions of the Institute for Astronomy, the University of Hawaii, the Pan-STARRS Project Office, the Max-Planck Society and its participating institutes, the Max Planck Institute for Astronomy, Heidelberg and the Max Planck Institute for Extraterrestrial Physics, Garching, The Johns Hopkins University, Durham University, the University of Edinburgh, Queen’s University Belfast, the Harvard-Smithsonian Center for Astrophysics, and the Las Cumbres Observatory Global Telescope Network, Incorporated, the National Central University of Taiwan, and the National Aeronautics and Space Administration under Grant No. NNX08AR22G issued through the Planetary Science Division of the NASA Science Mission Directorate.

The spectroscopic observations reported here were obtained at the MMT Observatory, a joint facility of the Smithsonian Institution and the University of Arizona. This paper uses data products produced by the OIR Telescope Data Center, supported by the Smithsonian Astrophysical Observatory, and we have benefited from NASA’s Astrophysics Data System Bibliographic Services and the SIMBAD database, operated at CDS, Strasbourg, France.

A. Finding Charts

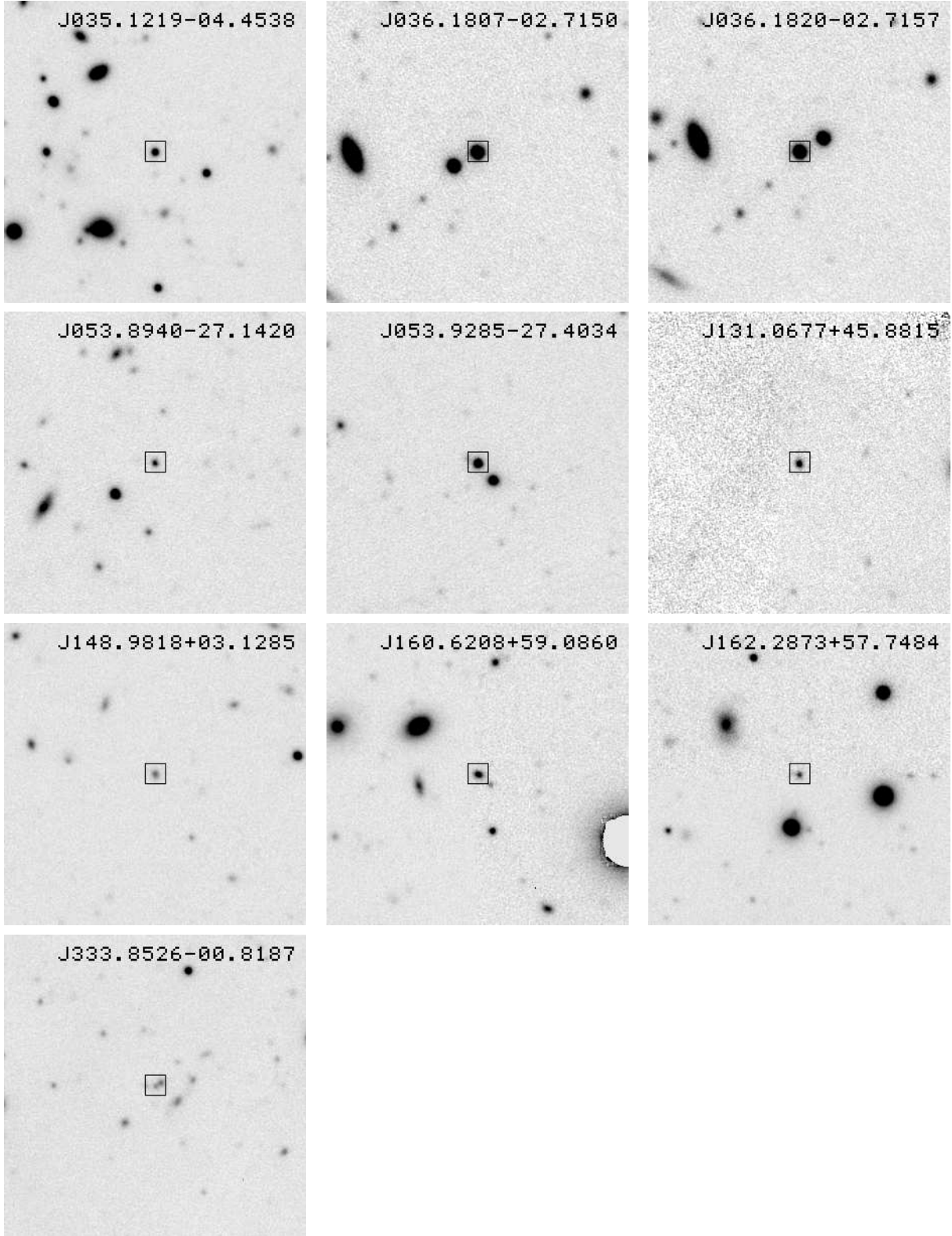


Fig. 8.— Finding charts for the objects in our candidate catalog that do not reside in the SDSS fields. North is up, East is left and the i_{p1} images are $1'$ on a side.

REFERENCES

- Bergeron, P., Saumon, D., & Wesemael, F. 1995, ApJ, 443, 764
- Bergeron, P. 2003, ApJ, 586, 201
- Bergeron, P., Ruiz, M. T., Hamuy, M., Leggett, S. K., Currie, M. J., Lajoie, C.-P., & Dufour, P. 2005, ApJ, 625, 838
- Bergeron, P. et al. 2011, ApJ, in press, arXiv:1105.5433
- Chambers, K. C, *et al.*, in preparation.
- Covey, K. R., et al. 2007, AJ, 134, 2398
- Eisenstein, D. J., et al. 2006, ApJS, 167, 40
- Fabricant, D., et al. 2005, PASP, 117, 1411
- Fukugita, M., et al. 1996, AJ, 111, 1748
- Hall, P. B., Kowalski, P. M., Harris, H. C., Awal, A., Leggett, S. K., Kilic, M., Anderson, S. F., & Gates, E. 2008, AJ, 136, 76
- Hambly, N. C., Smartt, S. J., & Hodgkin, S. T. 1997, ApJ, 489, L157
- Hansen, B. M. S. 1998, Nature, 394, 860
- Harris, H. C., et al. 2006, AJ, 131, 571
- High, F. W., Stubbs, C. W., Rest, A., Stalder, B., & Challis, P. 2009, AJ, **138**, 110.
- Hodapp, K. W., Siegmund, W. A., Kaiser, N., Chambers, K. C., Laux, U., Morgan, J., & Mannery, E. 2004, Proc. SPIE, **5489**, 667
- Kaiser, N., et al. 2010, Proc. SPIE, 7733, 12K.
- Kilic, M., et al. 2006, AJ, 131, 582
- Kilic, M., Kowalski, P. M., & von Hippel, T. 2009, AJ, 138, 102
- Kilic, M., et al. 2010, ApJ, 715, L21
- Kilic, M., et al. 2010, ApJS, 190, 77
- Koester, D., & Knist, S. 2006, A&A, 454, 951

- Kowalski, P. M., & Saumon, D. 2006, *ApJ*, 651, L137
- Kurucz, R. L. 1996, *M.A.S.S., Model Atmospheres and Spectrum Synthesis*, **108**, 2
- Lépine, S., & Shara, M. M. 2005, *AJ*, 129, 1483
- Leggett, S. K., Ruiz, M. T., & Bergeron, P. 1998, *ApJ*, 497, 294
- Liebert, J., Dahn, C. C., & Monet, D. G. 1988, *ApJ*, 332, 891
- Liebert, J., Bergeron, P., & Holberg, J. B. 2005, *ApJS*, 156, 47
- Liebert, J., Kilic, M., Williams, K. A., von Hippel, T., Winget, D. M. J., Harris, H. C., Levine, S., & Metcalfe, T. S. 2007, 15th European Workshop on White Dwarfs, 372, 129
- Magnier, E. 2006, *Proceedings of The Advanced Maui Optical and Space Surveillance Technologies Conference*, Ed.: S. Ryan, The Maui Economic Development Board, p.E5
- Magnier, E., *et al.*, in preparation.
- Marigo, P., Girardi, L., Bressan, A., Groenewegen, M. A. T., Silva, L., & Granato, G. L. 2008, *A&A*, 482, 883
- Mink, D. J., Wyatt, W. F., Caldwell, N., Conroy, M. A., Furesz, G., & Tokarz, S. P. 2007, *Astronomical Data Analysis Software and Systems XVI*, 376, 249
- Munn, J. A., *et al.* 2004, *AJ*, 127, 3034
- Onaka, P., Tonry, J. L., Isani, S., Lee, A., Uyeshiro, R., Rae, C., Robertson, L., & Ching, G. 2008, *Proc. SPIE*, **7014**, 12.
- Oppenheimer, B. R., Hambly, N. C., Digby, A. P., Hodgkin, S. T., & Saumon, D. 2001, *Science*, 292, 698
- Reid, I. N., Sahu, K. C., & Hawley, S. L. 2001, *ApJ*, 559, 942
- Robin, A. C., Reylé, C., Derrière, S., & Picaud, S. 2003, *A&A*, 409, 523
- Rowell, N., & Hambly, N. C. 2011, *MNRAS*, in press, arXiv:1102.3193
- Schechter, P. L., Mateo, M., & Saha, A. 1993, *PASP*, 105, 1342
- Stubbs, C. W., Doherty, P., Cramer, C., Narayan, G., Brown, Y. J., Lykke, K. R., Woodward, J. T., & Tonry, J. L. 2010, *ApJS*, 191, 376

Tremblay, P.-E., Bergeron, P., & Gianninas, A. 2011, ApJ, 730, 128

Tonry, J. L., Burke, B. E., Isani, S., Onaka, P. M., & Cooper, M. J. 2008, Proc. SPIE, **7021**, 9.

Tonry, J. L., *et al.*, in preparation.

Winget, D. E., Hansen, C. J., Liebert, J., Van Horn, H. M., Fontaine, G., Nather, R. E., Kepler, S. O., & Lamb, D. Q. 1987, ApJ, 315, L77

York, D. G., et al. 2000, AJ, 120, 1579